Fusion Engineering and Design 192 (2023) 113635

Contents lists available at ScienceDirect

Fusion Engineering and Design

journal homepage: www.elsevier.com/locate/fusengdes

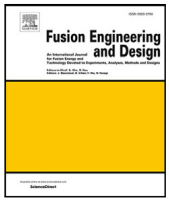

Control-oriented core-SOL-divertor model to address integrated burn and divertor control challenges in ITER

Vincent Graber *, Eugenio Schuster

Mechanical Engineering and Mechanics, Lehigh University, Bethlehem, PA 18015, USA

ARTICLE INFO

Keywords:
ITER
Scrape-off layer
Divertor
Burn control
Plasma modeling

ABSTRACT

The real-time regulation of a burning plasma's temperature and density, or burn control, will be necessary to produce high fusion power in future tokamaks like ITER. This is made more challenging due to the plasma's nonlinear characteristics and the interdependence between the core-plasma and edge-plasma regions. For example, a raising plasma temperature leads to increasing reactivity and therefore to more alpha-particle heating, which further increases temperature. Furthermore, a raise of the fusion power increases the heat flow through the scrape-off-layer (SOL), which can compromise the integrity of the divertor without proper safeguards. For control design, a model-based approach is attractive because it can directly incorporate the nonlinear, coupled, burning-plasma dynamics into the design. To facilitate this design approach, a control-oriented core-SOL-divertor (CSD) model is presented in this work. In this CSD model, a core-plasma model captures the nonlinear dynamics of the core's density and temperature, and a SOL-divertor model defines the plasma conditions at the separatrix and divertor including the heat load on the target plates. The core-plasma and SOL-divertor models are coupled through the exchange of various variables. In particular, the SOL-divertor model yields the separatrix temperature and the influx of recycled particles into the core-plasma. These variables influence the power and particle balances captured by the core-plasma model. In return, the core-plasma model determines the intensity of the heat and particles fluxes across the separatrix, and this outflow strongly impacts the SOL-divertor model. Therefore, the power and density of the core-plasma, which can be readily modulated through external heating systems and pellet injection, can be viewed as control knobs for the SOL-divertor region in addition to the gas puffing. In simulations of the CSD model, it is demonstrated how external actuation can be utilized to meet burn control and divertor control objectives simultaneously.

1. Introduction

For burning-plasma operations in ITER, careful regulation of the core-plasma's temperature and density, or burn control, will be necessary to produce high fusion powers. Real-time burn control can be achieved with model-based controllers [1–3], which directly incorporate the nonlinear, coupled dynamics of the burning plasma, that determine the amounts of auxiliary heating and external fueling needed to drive the plasma to desired regimes in temperature-density space [4–6]. The controller's requests for external heating and fueling can be met with the following ITER actuators: neutral beam injection, ion cyclotron heating, electron cyclotron heating, pellet injection, and gas injection. In prior work [7–9], it was shown that optimal allocation algorithms [10,11] can be employed to manage ITER's suite of actuator systems so that they produce the necessary quantities of external heating and fueling despite the actuators' dynamics and constraints. Both the nonlinear burn controller and the optimal actuator allocator [8,9], which work in tandem, used adaptive estimation techniques to overcome uncertainty in various complex phenomena such as the particle confinement time and the fueling source from wall-recycling (i.e., specific model parameters that were not known to the controller were estimated in real-time).

The burn controllers presented in [7–9] were based on control-oriented models that only included the plasma's core region. In [6], this core-plasma model was coupled to a two-point model [12] of the scrape-off-layer (SOL), which relates conditions at an upstream separatrix location to conditions at the divertor targets, and an analysis of ITER's operational limits in temperature-density space was performed. These operational limits included the maximum allowable heat load on ITER's tungsten divertor (10 MW/m^2 [13]). Because the heat load on the divertor increases with the power flowing across the separatrix, achieving burn control objectives, such as a high fusion power output,

* Corresponding author.
E-mail address: graber@lehigh.edu (V. Graber).

https://doi.org/10.1016/j.fusengdes.2023.113635
Received 31 October 2022; Received in revised form 2 March 2023; Accepted 4 March 2023

could threaten the integrity of the divertor. Various other coupled dynamics between the plasma's core and the SOL-divertor regions make integrated burn and divertor control more difficult. For example, SOL-divertor conditions determine the strength of the deuterium-tritium (DT) wall-recycling and the impurity pollution which effect the ion densities in the core-plasma region. Furthermore, divertor detachment depends strongly on the upstream separatrix density and the power flowing into the SOL from the core-plasma region.

This work presents a control-oriented core-SOL-divertor (CSD) model. It was developed to facilitate the design of nonlinear, model-based controllers that can achieve burn control and divertor control objectives simultaneously. The CSD model couples together three models for separate regions of the burning plasma: the core-plasma region, the SOL (the two-point model), and the divertor-plasma region. This model improves upon that presented in prior work [6] in a number of ways to make it more suitable for control design. Most significantly, this work adds a model for the neutral inventory in the divertor-plasma region. With this upgrade, the ionic outflow from the plasma's core, the divertor leakage into the plasma's core, the particle pumping from ITER's cyropumps, and external gas injection are now considered. In addition, the radiative cooling from impurities in the divertor-plasma region can now be regulated with impurity gas injection.

This paper is ordered as follows. The complete CSD model is presented in Section 2. Respectively, Sections 2.1, 2.2, and 2.3 provide the core, SOL, and divertor regions of the CSD model. In Section 3, the results from open-loop simulations demonstrate the potential that the CSD model has for nonlinear control design. Finally, conclusions and plans for future work are stated in Section 4.

2. The core-SOL-divertor model

The presented core-SOL-divertor (CSD) model is illustrated in Fig. 1. The CSD model includes a two-chamber model [12,14] that consists of two reservoirs: the core-plasma chamber (Section 2.1) and the divertor-plasma chamber (Section 2.3). The divertor-plasma chamber has a neutral-particle content of N^{div} that leaks at the rate of ϕ^D $particles/s$ into the vacuum surrounding the core-plasma chamber, and only a fraction γ^D of ϕ^D ends up contributing to the ionic fueling of the core-plasma chamber. The core-plasma chamber (the confined plasma bounded by the separatrix) with ion density n_i loses ions at the rate ϕ^+ into the scrape-off layer (SOL). Because the SOL is a conduit of particles and not a reservoir in this CSD model, the SOL immediately transfers the ionic outflow into the divertor-plasma chamber.

The two-chamber model is coupled to a two-point model of the SOL (Section 2.2) through the exchange of various parameters. The primary control knobs of the two-point model that originate from the core-plasma chamber are the power entering the SOL P_{SOL} and the separatrix density n_u. Both control knobs can be readily modulated with core-plasma actuators such as neutral beam injection and pellet injection. The two-point model outputs the separatrix temperature T_u as an input to the core-plasma chamber. The two-point model also determines the heat load on the divertor targets q_{dep}, the target temperature T_t, and the particle-recycling influx into the divertor-plasma chamber (ϕ^{rec}). Particles can also be injected into the divertor-plasma chamber through gas puffing, and pumping serves as a sink term in the divertor-plasma's neutral content. The concentration of impurities in the divertor-plasma chamber determines the radiative cooling below the X-point which is an input to the two-point model.

2.1. The core-plasma chamber

The domain of the core-plasma chamber is defined by the toroidal magnetic flux coordinate ψ where the magnetic axis is at $\psi = 0$ and the separatrix is at $\psi = \psi_0$. For burning plasmas in ITER, the radial profiles for the ion and electron temperatures are expected to be uncoupled and parabolic [15,16] such that

$$T_i(t,\psi) = (T_{i,0} - T_u)(1 - \psi/\psi_0)^2 + T_u, \tag{1}$$

$$T_e(t,\psi) = (T_{e,0} - T_u)(1 - \psi/\psi_0)^2 + T_u, \tag{2}$$

where $T_{i,0}$ and $T_{e,0}$ are the ion and electron temperatures at the magnetic axis. At the separatrix, the ion and electron temperatures are assumed to be the same at T_u.

The volume-averaged ion and electron energy densities are given by $E_i = \frac{3}{2} n_i \langle T_i \rangle$ and $E_e = \frac{3}{2} n_e \langle T_e \rangle$ where

$$\langle T_j(t)^k \rangle = \frac{1}{\psi_0} \int_0^{\psi_0} [(T_{j,0} - T_u)\left(1 - \frac{\psi}{\psi_0}\right)^2 + T_u]^k d\psi, \tag{3}$$

for $j \in \{i, e\}$. For $k = 1$, $\langle T_j^1 \rangle = \frac{1}{3} T_{j,0} + \frac{2}{3} T_u$. The total ion density n_i is the sum of the deuterium density n_D, the tritium density n_T, the alpha-particle density n_α, and the impurity density n_I. Because of the quasi-neutrality condition, the electron density is $n_e = n_D + n_T + 2n_\alpha + Z_I n_I$ where Z_I is the atomic number of the impurity species. Assuming that the particle density profiles are flat [15], $n_e(t,\psi) = n_e(t) = n_u$ where n_u is the separatrix density.

The ion and electron energy densities are governed by

$$\dot{E}_i = -\frac{E_i}{\tau_{E,i}} + f_i P_\alpha + P_{ei} + P_{aux,i}, \tag{4}$$

$$\dot{E}_e = -\frac{E_e}{\tau_{E,e}} + f_e P_\alpha - P_{ei} - P_{rad} + P_{ohm} + P_{aux,e}, \tag{5}$$

where each term is in units of W/m^3. Auxiliary power systems (e.g., neutral beam injectors) heat the ions and electrons at rates of $P_{aux,i}$ and $P_{aux,e}$, respectively. The ohmic heating and the radiation losses [17] are given by

$$P_{ohm} = 2.8 \times 10^{-9} Z_{eff} I_p^2 a^{-4} \langle T_e^{-\frac{3}{2}} \rangle, \tag{6}$$

$$P_{rad} = 5.5 \times 10^{-37} Z_{eff} n_e^2 \langle T_e^{\frac{1}{2}} \rangle, \tag{7}$$

where the temperature is in units of keV, $I_p = 15$ MA is the plasma current, $a = 2$ m is the plasma minor radius, and the effective atomic number is $Z_{eff} = (n_D + n_T + 4n_\alpha + Z_I^2 n_I)/n_e$. The collisional power exchange between the ions and electrons [17,18] is given by

$$P_{ei} = \frac{3}{2} n_e \frac{\langle T_e \rangle - \langle T_i \rangle}{\tau_{ei}}. \tag{8}$$

The energy relaxation time in (8) is determined by

$$\tau_{ei} = \frac{3\pi\sqrt{2\pi}\varepsilon_0^2 \langle T_e^{3/2} \rangle}{e^4 \sqrt{m_e} \ln \Lambda_j} \sum_p \frac{m_p}{n_p Z_p^2}, \tag{9}$$

where $e = 1.622 \times 10^{-19}$C, $m_e = 9.1096 \times 10^{-31}$kg, and $\varepsilon_0 = 8.854 \times 10^{-12}$F/m. With $T_{j,0}$ in units of Kelvin, $\Lambda_j = 1.24 \times 10^7 T_{j,0}^{3/2} / (n_e^{1/2} Z_{eff}^2)$ for $j \in \{i, e\}$. For the summation over $p \in \{\alpha, D, T, I\}$, m_p, Z_p, and n_p indicate the mass, atomic number, and density of each ion species. The alpha power P_α is proportional to the fusion reaction rate density $S_\alpha = n_D n_T \langle \sigma v \rangle$. Therefore, $P_\alpha = Q_\alpha S_\alpha$ where $Q_\alpha = 3.52$ MeV. The DT reactivity [19] is given by

$$\langle \sigma v \rangle = G(T_{i,0}) \times C_1 \omega \sqrt{\xi / (m_r c^2 T_{i,0}^3)} e^{-3\xi}, \tag{10}$$

$$\omega = T_{i,0} \left[1 - \frac{T_{i,0}(C_2 + T_{i,0}(C_4 + T_{i,0} C_6))}{1 + T_{i,0}(C_3 + T_{i,0}(C_5 + T_{i,0} C_7))} \right]^{-1},$$

where $\xi = (B_G^2 / 4\omega)^{1/3}$, $m_r c^2$, B_G, and C_l for $l \in \{1, \ldots, 7\}$ are constants. The temperature-dependent correction factor $G(T_{i,0})$ accounts for the volume-averaging procedure [4]. The fusion-born alpha particles unevenly heat the plasma's ions and electrons. In prior work [7], it was shown that the fraction of the alpha power deposited into the ions f_i in (4) can be modeled as [17,20]

$$\varepsilon_c = \frac{A_\alpha T_{e,0}}{m_e^{1/3} n_e^{2/3}} \sum_p \frac{n_p Z_p^2}{A_p} \left(\frac{3\sqrt{\pi} \ln \Lambda_i}{4 \ln \Lambda_e} \right)^{2/3}, \tag{11}$$

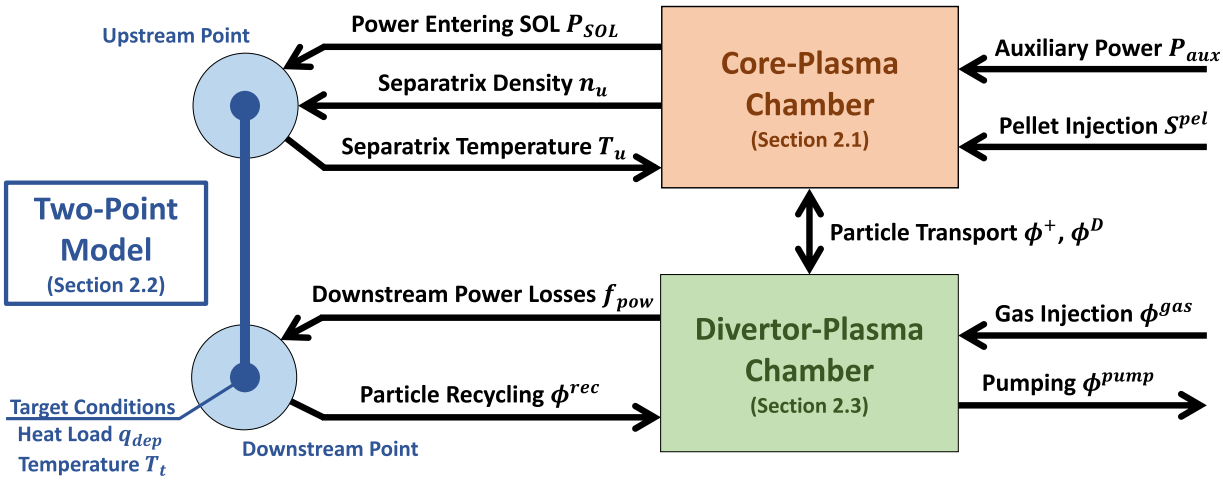

Fig. 1. The core-SOL-divertor (CSD) model couples of three different models: the core-plasma chamber (Section 2.1), the two-point model (Section 2.2), and the divertor-plasma chamber (Section 2.3). In the diagram, the black arrows indicate the various inputs and outputs for each of the models. The external actuators are the auxiliary heating, pellet injection, gas injection, and pumping.

$$f_i = \frac{1}{x_0}\left[\frac{1}{3}\ln\frac{1-x_0^{1/2}+x_0}{\left(1+x_0^{1/2}\right)^2} + \frac{2}{\sqrt{3}}\left(\tan^{-1}\frac{2x_0^{1/2}-1}{\sqrt{3}} + \frac{\pi}{6}\right)\right],$$

where $x_0 = \varepsilon_{\alpha_0}/\varepsilon_c$, $\varepsilon_{\alpha_0} = Q_\alpha$ is the fusion-born alpha particle's initial energy, and $A_\alpha = 4$ is its atomic mass. The summation is taken over the ion species $p \in \{\alpha, D, T, I\}$. In (5), the electron-heating fraction is $f_e = 1 - f_i$.

In (4) and (5), the ion and electron energy confinement times ($\tau_{E,i}$ and $\tau_{E,e}$) are proportional to the global energy confinement time τ_E such that $\tau_{E,i} = \zeta_i \tau_E$ and $\tau_{E,e} = \zeta_e \tau_E$ (ζ_i and ζ_e are constants). The IPB98(y,2) scaling law for H-mode plasmas [21,22] is

$$\tau_E = K H I_p^{0.93} R^{1.97} B^{0.15} M^{0.19} \epsilon^{0.58} \kappa^{0.78} \hat{n}_e^{0.41} P_{tot}^{-0.69}, \tag{12}$$

where $K = 0.0562$, H indicates the confinement quality of the plasma, $R = 6.2$ m is the plasma major radius, B is the toroidal magnetic field, $M = 3\gamma + 2(1-\gamma)$, $\gamma = n_T/(n_D + n_T)$, $\epsilon = a/R$, $\kappa = 1.7$ is the vertical elongation at the 95% flux surface, and $\hat{n}_e = n_e/10^{19}$. The listed values are for ITER. The plasma power balance gives the total power in MW:

$$P_{tot} = (P_{aux,i} + P_{aux,e} + P_\alpha + P_{ohm} - P_{rad})V \times 10^{-6}, \tag{13}$$

where $V = 840$ m^3 is the plasma volume in ITER. When the total plasma power P_{tot} (13) exceeds the threshold power scaling law $P_{thr} = 4.3 M^{-1} B^{0.772} (n_e/10^{20})^{0.782} R^{0.999} a^{0.975}$, the plasma transitions from L-mode to H-mode [23].

For (6)–(9), the solutions of (3) for $k = -3/2$, $k = 1/2$, and $k = 3/2$ can be found. With $T_\Delta = T_{e,0} - T_u$, they are

$$\langle T_e^{-\frac{3}{2}} \rangle = \frac{1}{T_u \sqrt{T_{e,0}}}, \tag{14}$$

$$\langle T_e^{\frac{1}{2}} \rangle = \frac{1}{2}\sqrt{T_{e,0}} + \frac{T_u}{2\sqrt{T_\Delta}} \ln\left|\frac{\sqrt{T_\Delta^2 + T_\Delta T_u} + T_\Delta}{\sqrt{T_\Delta T_u}}\right|, \tag{15}$$

$$\langle T_e^{\frac{3}{2}} \rangle = \frac{1}{4}T_{e,0}^{\frac{3}{2}} + \frac{3}{8}T_u\sqrt{T_{e,0}} - \frac{3}{8}\frac{T_u^2 \ln\sqrt{T_u}}{\sqrt{T_\Delta}} + \frac{3}{8}\frac{T_u^2}{\sqrt{T_\Delta}} \ln\left(\sqrt{T_\Delta} + \sqrt{T_{e,0}}\right). \tag{16}$$

An estimate for the volume-average of P_{ei} (8) is taken because finding a closed-form solution was not tractable. Since P_{ei} does not appear in the power balance (13), it does not directly influence τ_E or the power entering the SOL from the core-plasma chamber (see Section 2.2). Therefore, the impact of taking an estimative approach, which is comparable to that taken in [4], is minimal.

The response models for the particle densities are

$$\dot{n}_\alpha = -\frac{n_\alpha}{\tau_\alpha} + \frac{\gamma^D \phi_\alpha^D}{V} + S_\alpha, \tag{17}$$

$$\dot{n}_D = -\frac{n_D}{\tau_D} + \frac{\gamma^D \phi_D^D}{V} - S_\alpha + S_D^{pel}, \tag{18}$$

$$\dot{n}_T = -\frac{n_T}{\tau_T} + \frac{\gamma^D \phi_T^D}{V} - S_\alpha + S_T^{pel}, \tag{19}$$

$$\dot{n}_I = -\frac{n_I}{\tau_I} + \frac{\gamma^D \phi_I^D}{V} + S_I^{pel}, \tag{20}$$

where each term is in units of m^{-3}s^{-1}. The particle confinement times are proportional to (12) such that $\tau_p = \zeta_p \tau_E$ for $p \in \{\alpha, D, T, I\}$ (each ζ_p is constant). The particle fluxes (particles/s) flowing from the divertor-plasma chamber (Section 2.3) into the core-plasma chamber are denoted as $\gamma^D \phi_p^D$ for $p \in \{\alpha, D, T, I\}$ where $\gamma^D \ll 1$ is the shielding factor [14]. ITER's pellet injection systems introduce particles directly into the plasma's core at rates of S_D^{pel}, S_T^{pel}, and S_I^{pel}. The dynamics of the ITER actuators can be incorporated into the CSD model. For example, the aforementioned pellet injection systems were modeled in [9] to include a delay for the travel time of the pellets, and their fueling efficiencies were modeled to decrease with increasing plasma temperature. Furthermore, the neutral beam power, which enters as $P_{aux,i}$ and $P_{aux,e}$ in (4)–(5), was modeled to include a thermalization delay and uneven heating of the ion and electron populations. While these actuator dynamics could have been included in the presented CSD model, they were left out for brevity. In addition, the actuator dynamics in [9] were modeled separately from the plasma model such that they can be readily applied to the presented CSD model.

2.2. The two-point model

Connecting upstream separatrix conditions (at the outer-midplane) to downstream separatrix conditions at the divertor target, the two point model [12] is defined by particle, pressure and power balances along the SOL:

$$2 n_t T_t = f_{mom} n_u T_u, \tag{21}$$

$$T_u^{7/2} = T_t^{7/2} + \frac{7}{2}\frac{f_{cond} q_\parallel L}{\kappa_0}, \tag{22}$$

$$(1 - f_{pow}) q_\parallel = \gamma_s n_t T_t c_{st}, \tag{23}$$

where n_u and n_t are the upstream and downstream densities, T_u and T_t are the upstream and downstream temperatures, $q_\parallel$ is the parallel power flux density, $\kappa_0 = 2000$ is the parallel conductivity coefficient, $\gamma_s = 7$ is the sheath heat transmission coefficient, c_{st} is the plasma sound speed, and L is the connection length (half of the along-field distance between the two divertor plates). The correction factors f_{cond}, f_{mom}, and f_{pow} model the inclusion of convection, frictional collisions with neutrals, and radiation and charge exchange losses below the X-point, respectively.

In [12], the two-point model (21)–(23) was reformulated in terms of the upstream separatrix density n_u (m^{-3}) and the power flowing across the separatrix from the plasma's core into the SOL P_{SOL} (W). With flat radial density profiles, $n_u = n_e$ can be readily controlled with DT pellet injection into the plasma's core (S_D^{pel} and S_T^{pel} from (18) and (19)). The power flowing into the SOL is given by $P_{SOL} = P_{tot} \times 10^6$ from (13). It can be readily controlled with external heating into the plasma's core ($P_{aux,i}$ and $P_{aux,e}$ from (4) and (5)). Alternatives to regulating the power balance (13) include impurity pellet injection [24] to increase P_{rad} (7) and isotopic fuel tailoring [2] to decrease P_α by changing the tritium fraction $\gamma = n_T/(n_D + n_T)$. Therefore, n_u and P_{SOL}, outputs of the core-plasma chamber, can be viewed as control knobs for the two-point model.

The upstream separatrix temperature T_u is an input to the core-plasma chamber (1)–(2) that is given by

$$T_u = \left(\left(\frac{7^2}{8^2 \pi^3} \right) \frac{f_{cond} P_{SOL}^2 L}{e n_u \chi_\perp^{SOL} \kappa_0 a R^2 (B_\theta/B)_u} \right)^{2/9}, \tag{24}$$

where T_u is calculated to be in eV, $\chi_\perp^{SOL}$ is the anomalous cross-field heat thermal diffusivity, and $(B_\theta/B)_u$ and $(B_\theta/B)_t$ are ratios of the poloidal field over the total field at the upstream and downstream locations, respectively. The expected values for ITER [25,26] are $L = 75$ m, $\chi_\perp^{SOL} = 1$ m^2 s^{-1}, $(B_\theta/B)_u = 0.3$, and $(B_\theta/B)_t = 0.075$. The downstream (i.e., on the divertor target) temperature (eV) is given by

$$T_t = 2.67 \times 10^{-3} \left(\frac{(1 - f_{pow})^2}{f_{mom}^2 f_{cond}^{\frac{8}{9}}} \right) \left(\frac{m_i}{\gamma_s^2 e^{\frac{37}{9}}} \right) \times \frac{P_{SOL}^{\frac{20}{9}} \kappa_0^{\frac{8}{9}}}{n_u^{\frac{28}{9}} (\chi_\perp^{SOL})^{\frac{10}{9}} L^{\frac{8}{9}} (B_\theta/B)_u^{\frac{10}{9}} a^{\frac{10}{9}} R^{\frac{20}{9}}}. \tag{25}$$

The average ion mass is given by $m_i = \sum_p n_p m_p / n_i$ for $p \in \{\alpha, D, T, I\}$. Phenomena that are characteristic of the detached regime, such as ion-neutral friction, become more significant at low T_t [12]. Therefore, divertor detachment is assumed to be achieved when the target temperature falls below $T_t \leq 7$ eV [27] in the presented CSD model.

The peak heat load on the targets (W/m^2) is given by

$$q_{dep} = 1.61 \times 10^{-2} (\cos\beta) (f_{cond})^{-\frac{2}{9}} \frac{(B_\theta/B)_t}{(B_\theta/B)_u} \times \left(\frac{P_{SOL}^2}{e n_u \chi_\perp^{SOL}} \right)^{\frac{7}{9}} \left(\frac{\kappa_0^{\frac{2}{9}} (B_\theta/B)_u^{\frac{2}{9}}}{L^{\frac{2}{9}} R^{\frac{14}{9}} a^{\frac{7}{9}}} \right). \tag{26}$$

To avoid damaging ITER's divertor targets, the power flux density should be kept below 10 MW/m^2 [13]. The term $\cos\beta$ accounts for target slanting which can reduce the plasma wetted area A_{wet}. The angle between the target's surface and the connecting magnetic field lines is complementary to the effective angle β. The plasma wetted area (m^2) on the targets is given by

$$A_{wet} = 4\pi R \left(\frac{(B_\theta/B)_u}{(B_\theta/B)_t} \right) \lambda_{q\parallel} (\cos\beta)^{-1}, \tag{27}$$

where the power decay length (m) is

$$\lambda_{q\parallel} = (f_{cond}^{2/9}) \frac{8^{5/9} \pi^{4/3}}{7^{5/9}} (e n_u \chi_\perp^{SOL})^{7/9} P_{SOL}^{-5/9} \kappa_0^{-2/9} L^{2/9} \times (B_\theta/B)_u^{-2/9} a^{7/9} R^{5/9}. \tag{28}$$

Deuterium, tritium, and helium particles recycle at a rate of (particles/s):

$$\phi_p^{rec} = R^{rec} \times \Gamma_{p,t} \times (B_\theta/B)_t A_{wet}, \tag{29}$$

where $p \in \{\alpha, D, T\}$, R^{rec} is the recycling coefficient that models the wall-pumping effect. For $p \in \{\alpha, D, T\}$, the particle flux densities (m^{-2}s^{-1}) at the target are given by

$$\Gamma_{p,t} = \frac{7^{1/3} \pi}{2} \left(\frac{f_{mom}^2 f_{cond}^{2/3}}{(1 - f_{pow})} \right) \left(\frac{\gamma_s e^{7/3}}{m_p} \right) \times \left(\frac{n_p^7 L^2 a R^2 \chi_\perp^{SOL} (B_\theta/B)_u}{P_{SOL}^2 \kappa_0^2} \right)^{1/3}. \tag{30}$$

The recycling sources (29) are inputs to the model of the divertor-plasma chamber (Section 2.3).

TOKAM3X-EIRENE simulations of WEST have been shown to agree with the two-point model when appropriate values are used for the correction factors [28]. In the detached regime, $f_{cond} = 1$, $f_{mom} = 0.2$, and $f_{pow} = 0.5$ for the specific plasma studied in [28]. In the attached regime, $f_{cond} = 1$, $f_{mom} = 0.8$, and $f_{pow} = 0.1$. In the presented CSD model, the assumption is made that both f_{cond} and f_{mom} are constant, while f_{pow} is variable. The correction factor for the downstream radiative power losses [12,27] is modeled as

$$f_{pow} = 1 - \left(1 - \frac{14 c_Z L_Z n_u^2 L}{3 q_\parallel} \right)^{1/2}, \tag{31}$$

where the parallel power flux density (W/m^2) is given by

$$q_\parallel = \frac{7^{\frac{5}{9}}}{8^{\frac{11}{9}} \pi^{\frac{7}{3}} f_{cond}^{\frac{2}{9}}} \left(\frac{P_{SOL}^2}{e n_u \chi_\perp^{SOL}} \right)^{7/9} \times \left(\frac{\kappa_0^{\frac{2}{9}}}{L^{\frac{2}{9}} (B_\theta/B)_u^{\frac{7}{9}} R^{\frac{14}{9}} a^{\frac{7}{9}}} \right), \tag{32}$$

and the average radiative cooling rate L_Z is assumed to be 10^{-33} W/m^3 [29]. The downstream impurity concentration c_Z is an output from the divertor-plasma chamber (Section 2.3).

2.3. The divertor-plasma chamber

The divertor-plasma chamber consists of balance equations for the neutral-particle inventories [12,14]:

$$\dot{N}_\alpha^{div} = \phi_\alpha^+ - \gamma^D \phi_\alpha^D - \phi_\alpha^{pump} + \phi_\alpha^{rec}, \tag{33}$$

$$\dot{N}_D^{div} = \phi_D^+ - \gamma^D \phi_D^D - \phi_D^{pump} + \phi_D^{rec} + \phi_D^{gas}, \tag{34}$$

$$\dot{N}_T^{div} = \phi_T^+ - \gamma^D \phi_T^D - \phi_T^{pump} + \phi_T^{rec} + \phi_T^{gas}, \tag{35}$$

$$\dot{N}_I^{div} = \phi_I^+ - \gamma^D \phi_I^D - \phi_I^{pump} + \phi_I^{gas}, \tag{36}$$

where each term is in units of $particles/s$, and N_p^{div} for $p \in \{\alpha, D, T, I\}$ are the neutral-particle populations in the divertor-plasma chamber. From (17)–(20) in the core-plasma chamber model (Section 2.1), $\phi_p^+ \equiv {}^{n_p}/_{\tau_p} \times V$ for $p \in \{\alpha, D, T, I\}$ are the ionic outflows across the separatrix. The external gas puffing rates for fueling and impurity injection are given by ϕ_D^{gas}, ϕ_T^{gas}, and ϕ_I^{gas}. The recycling sources ϕ_α^{rec}, ϕ_D^{rec}, and ϕ_T^{rec} are given by (29) in Section 2.2.

The influxes of particles from the divertor-plasma chamber to the core-plasma chamber (Section 2.1) are given by $\gamma^D \phi_p^D = \gamma^D N_p^{div}/\tau^D$ for $p \in \{\alpha, D, T, I\}$ (these terms appear in (17)–(20)) where τ^D is the divertor retention time. Particles are also removed from the divertor-plasma chamber (and the two-chamber model as a whole) through pumping. While the cyropumps in ITER will be able to ramp their speed in real-time from 0 to 100% in 10 s [30], the overall effectiveness of the pumping is dependent on the local neutral pressure. Therefore, the pumping losses can be modeled as $\phi_p^{pump} = N_p^{div}/\tau^{pump}$ for

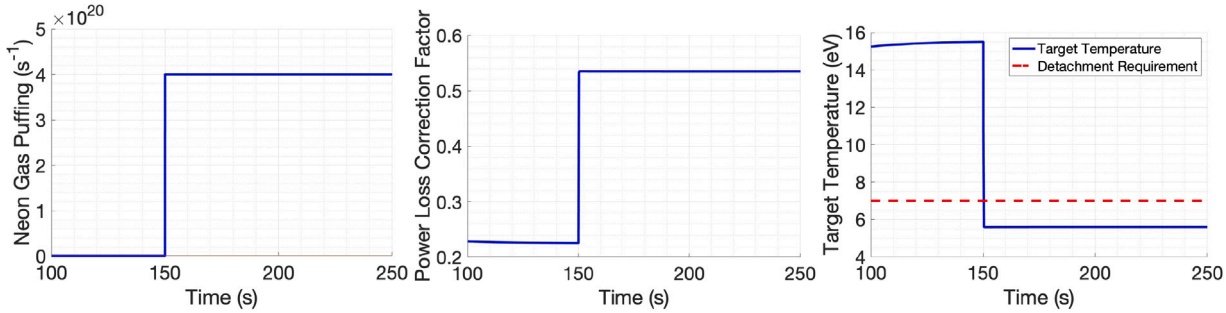

(a) Neon gas injection (ϕ_I^{gas}) increases the power losses (f_{pow}) which causes the target temperature (T_t) to meet the divertor detachment requirement.

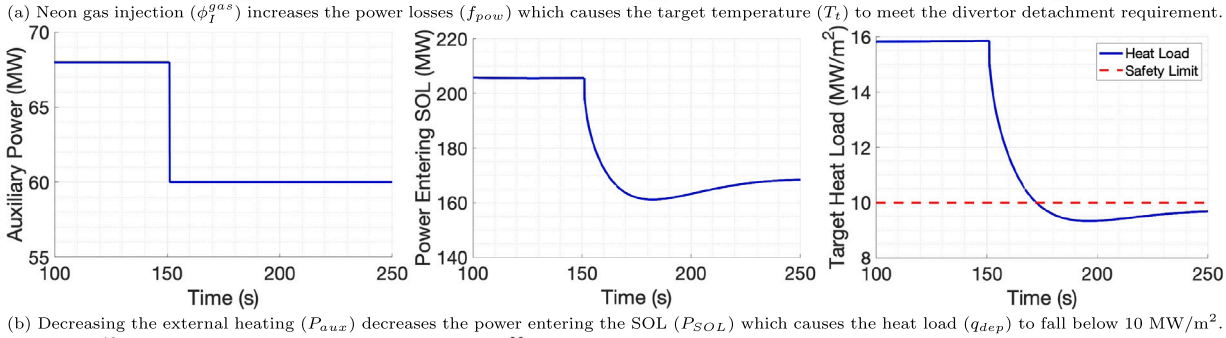

(b) Decreasing the external heating (P_{aux}) decreases the power entering the SOL (P_{SOL}) which causes the heat load (q_{dep}) to fall below 10 MW/m^2.

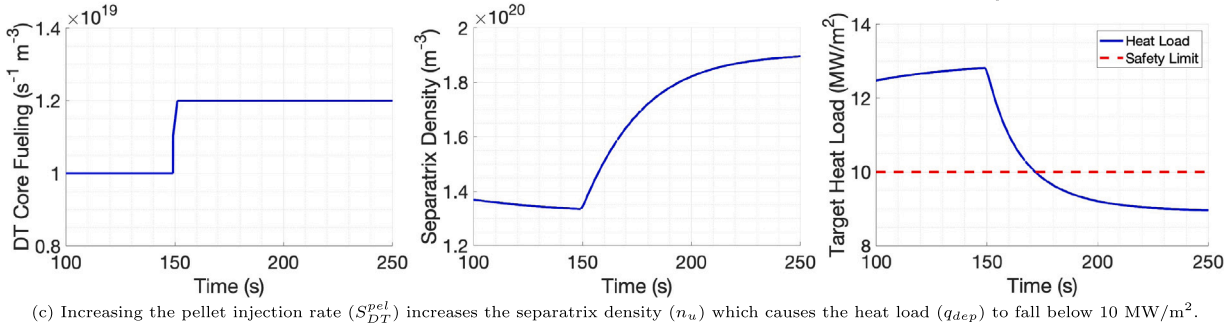

(c) Increasing the pellet injection rate (S_{DT}^{pel}) increases the separatrix density (n_u) which causes the heat load (q_{dep}) to fall below 10 MW/m^2.

Fig. 2. Simulation (a) shows how impurity gas puffing can be used to achieve divertor detachment in the core-SOL-divertor (CSD) model (Section 2) by lowering the target temperature below 7 eV. Simulations (b) and (c) show how external core-plasma actuation (auxiliary heating and pellet injection) can be employed to tune the "control knobs" of the two-point model (the power entering the SOL and the separatrix density) in order to protect the divertor target from high heat loads.

$p \in \{\alpha, D, T, I\}$ where τ^{pump} is the characteristic pumping time. Both τ^D and τ^{pump} are phenomenological quantities that absorb unknown relations. Their values can be obtained by fitting the model to experimental data or transport simulations. For example in [14], 1–D simulations were used to obtain $\tau^D = 80$ ms (for neon) and $\tau^{pump} = 100$ ms (for argon) for specific DIII-D plasmas with NBI heating. In addition, nonlinear adaptive control techniques [7,8] can be employed to estimate τ^D and τ^{pump} in real-time.

In Section 2.2, the correction factor for the power losses along the SOL (31) depends on the concentration of the impurities in the divertor-plasma chamber which includes both helium and the Z_I impurity (e.g., neon):

$$c_Z = \frac{N_{impurities}^{div}}{N_{total}^{div}} = \frac{N_\alpha^{div} + N_I^{div}}{N_\alpha^{div} + N_D^{div} + N_T^{div} + N_I^{div}}. \tag{37}$$

3. Simulation study of core-SOL-divertor model

Using the presented CSD model (Section 2), three simulations were completed to illustrate how external actuation can be employed to meet divertor control objectives. All three simulations were open-loop such that the outputs of the external actuators were predefined before the start of the simulation (i.e., an algorithm was not controlling the actuators in real-time). The impurity species was neon ($Z_I = 10$) which will be available for both pellet and gas injection in ITER [30] (impurity pellet injection was not used in these simulations). The constants defining the core-plasma's confinement qualities were set to $H = 1.1$, $\zeta_i = 1.15$, $\zeta_e = 0.85$, $\zeta_\alpha = 6$, $\zeta_D = 3$, $\zeta_T = 3$, and $\zeta_I = 8.7$. The following constants that are relevant to the SOL and divertor-plasma were set to $\beta = 85°$, $\gamma^D = 0.01$, $R^{rec} = 0.01$, $\tau^{pump} = 0.05$ s, $\tau^D = 0.5$ s, $f_{mom} = 0.8$, and $f_{cond} = 1$.

The primary results of the simulations are shown in Fig. 2. In simulation (a), the objective is to bring the divertor-plasma to the detached regime. This is achieved by injecting neon gas (ϕ_I^{gas}) into the divertor-plasma chamber (36) which increases the divertor-plasma's impurity concentration (37). The injected neon improves the radiative cooling (31) which drops target temperature (25) below 7 eV. The drawback of using neon gas puffing to transition from the attached regime to the detached regime is that some of the neon will leak into the core-plasma chamber and possibly erode the fusion power production.

In both simulation (b) and simulation (c), the objective is to drop the heat load on the divertor targets (26) below the safety limit of 10 MW/m^2. The approach in both simulations is to control the conditions in the SOL and divertor-plasma regions through the use of external core-plasma actuation. In simulation (b), the total auxiliary heating ($P_{aux} = P_{aux,i} + P_{aux,e}$) into the core-plasma (4)–(5) is lowered so that the power flowing across the separatrix into the SOL ($P_{SOL} = P_{tot}$ from (13)) decreases. This is rapidly drops the heat load on the target below the safety limit because $q_{dep} \propto P_{SOL}^{14/9}$. In simulation (c), the DT pellet injection ($S_{DT}^{pel} = S_D^{pel} + S_T^{pel}$) into the core-plasma (18)–(19) is increased so that the separatrix density (n_u) rises and the heat load falls below 10 MW/m^2.

4. Conclusions and future work

The open-loop simulations in Section 3 show how the control knobs of the SOL-divertor plasma, the power entering the SOL and the separatrix density, can be manipulated with core-plasma actuation systems (e.g., neutral beam injection and pellet injection) to meet divertor control objectives. Because the presented core-SOL-divertor (CSD) model is control-oriented, it can be used to facilitate the development of nonlinear burn controllers. Therefore, future work will be done to design nonlinear, model-based controllers that can address integrated burn and divertor control challenges. Furthermore, adaptive control techniques may be employed to overcome the uncertainty in quantities such as the divertor retention time (τ^D).

The presented CSD model can be further developed in a number of ways. Firstly, the characteristic pumping time τ^{pump} (Section 2.3) can be modeled to be inversely proportional to the controllable pumping speed of ITER's cyropumps. Secondly, the impurity sputtering source from the particle bombardment [31] on ITER's tungsten divertor can be added to the divertor-plasma chamber model (Section 2.3). Thirdly, the CSD model can be fitted to high-fidelity physics simulations of ITER to obtain phenomenological quantities such as τ^D, R^{rec}, and γ^D.

Declaration of competing interest

The authors declare that they have no known competing financial interests or personal relationships that could have appeared to influence the work reported in this paper.

Data availability

The authors are unable or have chosen not to specify which data has been used.

Acknowledgments

This material is based upon work supported by the U.S. Department of Energy, Office of Science, Office of Fusion Energy under Award Number DE-SC-0010661, and it was carried out in part under the ITER Scientist Fellow Network program.

References

[1] E. Schuster, et al., Burn control in fusion reactors via nonlinear stabilization techniques, Fusion Sci. Technol. 43 (1) (2002).
[2] M. Boyer, E. Schuster, Nonlinear burn condition control in tokamaks using isotopic fuel tailoring, Nucl. Fusion 55 (8) (2015).
[3] A. Pajares, E. Schuster, Robust nonlinear burn control in ITER to handle uncertainties in the fuel-line concentrations, Nucl. Fusion 59 (9) (2019).
[4] J. Martinell, J. Vitela, An optimal burn regime in a controlled tokamak fusion power plant, in: IEEE Transactions on Plasma Science, vol. 44, 2016, pp. 296–305.
[5] V. Graber, E. Schuster, Tritium-concentration requirements in the fueling lines for high-Q operation in ITER, in: European Physical Society, Milan, Italy, 2019.
[6] V. Graber, E. Schuster, Assessment of the burning-plasma operational space in ITER by using a control-oriented core-SOL-divertor model, Fusion Eng. Des. (ISSN: 0920-3796) 171 (2021).
[7] V. Graber, E. Schuster, Nonlinear adaptive burn control and optimal control allocation of over-actuated two-temperature plasmas, in: American Control Conference, Denver, USA, 2020.
[8] V. Graber, E. Schuster, Nonlinear burn control in ITER using adaptive allocation of actuators with uncertain dynamics, Nucl. Fusion 62 (2) (2022).
[9] V. Graber, E. Schuster, Actuator allocation with adaptive estimation of time-varying uncertain parameters for nonlinear burn control, in: IEEE Conference on Control Technology and Application, Trieste, Italy, 2022.
[10] O. Harkegard, S. Glad, Resolving actuator redundancy – optimal control vs. control allocation, Automatica 49 (2013) 1087–1103.
[11] J. Tjonnas, T. Johansen, Optimizing adaptive control allocation with actuator dynamics, in: IEEE Conference on Decision and Control, 2007, pp. 3780–3785.
[12] P.C. Stangeby, The Plasma Boundary, IOP, Bristol, 2000.
[13] G.W. Pacher, et al., ITER operation window determined from mutually consistent core–SOL–divertor simulations: definition and application, Nucl. Fusion 48 (10) (2008) 105003.
[14] J. Roth, et al., Divertor retention for recycling impurities, Nucl. Fusion 32 (10) (1992) 1835–1844.
[15] M. Shimada, et al., Physics design of ITER-FEAT, J. Plasma Fusion Res. 3 (2000) 77–83.
[16] R.W. Harvey, et al., Electron cyclotron heating and current drive in ITER, Nucl. Fusion 37 (1) (1997).
[17] J. Wesson, Tokamaks, second ed., Clarendon Press, Oxford, 1997.
[18] R. Gross, Fusion Energy, Wiley-Interscience, New York, 1984.
[19] H. Bosch, G. Hale, Improved formulas for fusion cross-sections and thermal reactivities, Nucl. Fusion 32 (4) (1992).
[20] D. Gallart, et al., Modelling of ICRF heating in DEMO with special emphasis on bulk ion heating, in: AIP Conf Proc, vol. 1689, 2015.
[21] M. Shimada, et al., Chapter 1: Overview and summary, Nucl. Fusion 47 (2007).
[22] E.J. Doyle, et al., Chapter 2: Plasma confinement and transport, Nucl. Fusion 47 (2007).
[23] Y.R. Martin, et al., Power requirement for accessing the H-mode in ITER, J. Phys.: Conf. Ser. 123 (2008).
[24] V. Graber, E. Schuster, Nonlinear adaptive burn control of two-temperature tokamak plasmas, in: IEEE Conference on Decision and Control, Nice, France, 2019.
[25] C.S. Pitcher, P.C. Stangeby, Experimental divertor physics, Plasma Phys. Control. Fusion 39 (1997).
[26] R.A. Pitts, et al., Physics basis for the first ITER tungsten divertor, J. Nucl. Mater. Energy 20 (2019).
[27] J. Le, Z. Sizheng, Investigation of divertor detachment in EAST by two-point model, Plasma Sci. Technol. 9 (2007).
[28] D. Fan, Y. Marandet, et al., Self-consistent coupling of the three-dimensional fluid turbulence code TOKAM3X and the kinetic neutrals code EIRENE, Contributions Plasma Phys. 58 (2018).
[29] A. Mavrin, Radiative cooling rates for low-Z impurities in non-coronal equilibrium state, J. Fusion Energy 36 (2017) 161–172.
[30] J. Snipes, et al., Actuator and diagnostic requirements of the ITER plasma control system, Fusion Eng. Des. 87 (12) (2012).
[31] R. Behrisch, W. Eckstein, Sputtering By Particle Bombardment, Springer, Berlin, 2007.